

Polytype-Dependent Upconversion

Photoluminescence in 3R-MoS₂

Omri Meron,^{†,‡,§} Idan Kizel,^{*,†,‡,§} Dror Hershkovitz,[†] Youngki Yeo,[†] Nirmal Roy,[†]
Wei Cao,[¶] Moshe Ben Shalom,[†] and Haim Suchowski^{†,‡}

[†]*Condensed Matter Physics Department, School of Physics and Astronomy, Tel Aviv University, Israel*

[‡]*Center for Light-Matter Interaction, Tel Aviv University, Israel*

[¶]*State Key Laboratory of Materials-Oriented Chemical Engineering, College of Chemical Engineering, Nanjing Tech University, China*

[§]*These authors contributed equally to this work.*

E-mail: idankizel@mail.tau.ac.il

Abstract

Ferroelectric van der Waals materials offer switchable polarization states, yet optical readout of their stacking configurations remains challenging. Here, building on the resonant exciton-exciton annihilation (EEA) mechanism recently identified in 2H-phase TMDs, we report the first observation of upconversion photoluminescence (UPL) in rhombohedral MoS₂ and demonstrate that this many-body process is strongly polytype-dependent. Using low-temperature spectroscopy, we observe anti-Stokes emission with superlinear power dependence characteristic of EEA. Beyond serving as an accurate layer-number sensor due to discrete bandgap variations, UPL provides a sensitive probe of stacking order across thicknesses. Trilayer ABA and BAB polytypes, which remain indistinguishable by surface potential measurements and second harmonic generation, exhibit markedly different UPL intensities, and this sensitivity persists in thicker

samples where multiple configurations coexist. First-principles calculations attribute this polytype dependence to modulation of the Γ -point conduction manifold, which controls energy-matching conditions for the annihilation process. Power-dependent spectroscopy further disentangles two distinct annihilation channels originating from different dark exciton valleys, identified through their contrasting intensity scaling and opposite density-induced energy shifts. Crucially, the annihilation process doubles the energy separation of nearly degenerate dark excitons while converting their weak emission into bright signal, providing experimental access to valley-specific responses that are obscured in direct dark-exciton spectroscopy. Our findings demonstrate that ferroelectric configurations provide a new degree of freedom for controlling nonlinear optical processes, with implications for all-optical ferroelectric readout and electrically switchable wavelength conversion in two-dimensional materials.

Keywords

Polar van der Waals (vdW) polytypes, SlideTronics, 2D ferroelectric materials, rhombohedral molybdenum disulfide, photoluminescence, upconversion

Introduction

The coupling between ferroelectric order and optical response in two-dimensional materials opens new pathways for controlling light-matter interactions at the nanoscale. In this context, two-dimensional (2D) transition metal dichalcogenides (TMDs) are particularly promising: their reduced dimensionality and strong Coulomb interactions yield robust excitonic effects, while their structural polymorphism enables tunable electronic phases.^{1,2} Rhombohedral (3R) polytypes of TMDs exemplify this promise, hosting interfacial ferroelectricity where interlayer sliding induces robust, switchable out-of-plane polarization, a property that underpins the emerging field of *SlideTronics*.^{3,4} At the same time, the strong

excitonic resonances and rich manifold of bright and dark excitons in few-layer TMDs⁵ give rise to a pronounced optical response, so that exciton recombination can be used as a sensitive optical probe of the underlying TMD properties.^{6,7}

Upconversion photoluminescence (UPL) in TMDs has been observed through several mechanisms, including phonon-assisted anti-Stokes emission,⁸⁻¹⁰ Auger-like scattering of bright excitons,^{11,12} and plasmon-enhanced dark exciton pathways.¹³ Recently, Chen *et al.* reported an efficient unique pathway: resonant exciton-exciton annihilation (EEA) of momentum-dark excitons gives rise to a pronounced UPL emission in few-layer 2H-TMDs.¹⁴

However, the manifestation of such upconversion pathways in rhombohedral TMDs has not yet been studied. In these systems, distinct ferroelectric polytypes (different layer-stacking sequences with different out-of-plane polarizations) have not yet been explored in the context of UPL, leaving open the question of whether upconversion is sensitive to the underlying stacking order and thus polytype dependent. Clarifying this connection is particularly relevant because 3R-TMDs combine switchable polarization with reconfigurable domain architectures,¹⁵ offering potential for devices that integrate wavelength conversion with ferroelectric control.

Here, we report the first observation of UPL in 3R-MoS₂ and demonstrate strong polytype dependence of the upconversion efficiency. We focus first on rhombohedral trilayers, where three distinct polytypes coexist: ABC/CBA (flipped same polytype, carrying opposite polarizations) and centrosymmetric ABA/BAB (both with zero net polarization). While ABC and CBA are distinguishable by Kelvin probe force microscopy (KPFM), the ABA and BAB configurations remain degenerate to such measurement. By contrast, our UPL readout converts their opposite symmetry into a robust difference in upconversion efficiency, enabling reliable, large-area labeling of ABA versus BAB. We then present first-principles calculations that attribute this polytype dependence to variations in the Γ -point conduction manifold governing the exciton-exciton annihilation process. We further map the layer and power dependence of the upconverted emission in few-layer stacks, disentangling two distinct

annihilation channels, each fed by a different dark exciton valley, through their contrasting intensity scaling and opposite density-induced shifts. Finally, we show that polytype-selective UPL persists in thicker samples where multiple polytypes coexist. This UPL-based readout complements recently established methods for mapping ferroelectric polytypes in rhombohedral TMDs.^{6,7,16} Together, these optical techniques provide non-invasive, large-area characterization that overcomes limitations of traditional surface potential measurements, while the coupling of UPL efficiency to switchable stacking order suggests a route toward slidetronic control of wavelength upconversion.

Results and Discussion

Polytype-resolved upconversion in trilayer 3R-MoS₂

We begin by demonstrating polytype-dependent UPL in the simplest thickness where multiple 3R polytypes show measurable UPL. In trilayer 3R-MoS₂, three distinct stacking configurations are possible, ABC (and its inverted partner CBA), and two Bernal-3R variants, ABA and BAB. As sketched in Figure 1a, ABC and CBA carry equal-magnitude but opposite out-of-plane polarization, whereas both ABA and BAB have zero net out-of-plane polarization.

Our trilayer device (90 nm-thick SiO₂/Si substrate) contains all three polytypes within a single contiguous flake, enabling a direct comparison under identical dielectric and excitation conditions. All UPL measurements in this work are performed at 4 K under continuous-wave 532 nm excitation. A conventional optical microscope image (Figure 1b) allows us to determine the layer number but offers no contrast between different stacking configurations. In contrast, the Kelvin probe force microscopy (KPFM) map (Figure 1c) resolves three surface-potential levels: two domains with opposite polarization contrast, ABC and CBA, and a third neutral level corresponding to the Bernal-3R family, either ABA or BAB, which cannot be distinguished.

To resolve the two Bernal-3R stackings, we perform a raster scan of the photoluminescence intensity across the same region (Figure 1d). The photoluminescence map effectively splits the KPFM-degenerate Bernal domain into two subdomains, allowing us to distinguish ABA from BAB. As shown in the representative spectra in Figure 1e, the two domains exhibit a measurable shift and splitting in the bright A-exciton resonance. This provides a further demonstration of the mechanism recently identified by Liang *et al.*, where the distinct dielectric environments of the substituent layers in ABA versus BAB stacking lift the excitonic degeneracy.¹⁶ Crucially, however, we identify that the UPL response provides another pronounced distinction between these two configurations. While the dark excitons (Figure 1e, left inset), associated with $Q - \Gamma / K - \Gamma$ transitions, show a uniform response, the UPL band (Figure 1e, right inset) reveals a dramatic difference in emission efficiency between the two neutral polytypes. This discrepancy, where the upconverted signal varies despite a constant dark-exciton reservoir, strongly implies that the polytype dependence originates from the nonlinear resonant characteristics of the EEA process.¹⁴ In the following subsection, we interpret these trends in terms of dark-exciton annihilation and the layer-resolved Γ -conduction manifold, establishing UPL as a sensitive, high-contrast probe for distinguishing these otherwise degenerate ferroelectric states.

Band structure origin of polytype-dependent UPL

The stark contrast in UPL efficiency across polytypes suggests a mechanism governed by the specific details of the rhombohedral electronic structure. While the bright A-exciton response follows the dielectric screening model proposed by Liang *et al.*,^{7,16} the UPL behavior requires a description of the many-body dynamics. Building on the resonant EEA framework recently established for 2H-TMDs,¹⁴ we attribute the UPL in 3R-MoS₂ to a process where two dark excitons with opposite momenta ($Q - \Gamma$ and $Q -' \Gamma$ or $K - \Gamma$ and $K -' \Gamma$) annihilate into a high-energy excitonic state near the Γ point (Figure 2a). Notably, in contrast to 2H-MoS₂ where the Q valley forms the conduction band minimum for thicknesses beyond

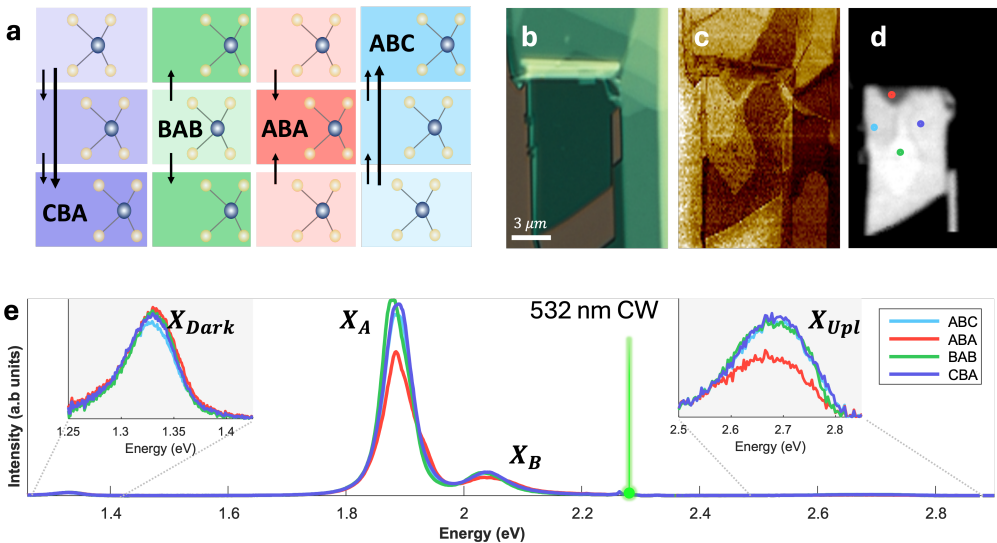


Figure 1: **Polytype-dependent UPL in trilayer 3R-MoS₂.** (a) Schematic of the four trilayer 3R stacking sequences (ABC, ABA, BAB, CBA), illustrating the relative layer registry and the associated out-of-plane polarization direction (arrows). (b) Optical micrograph image of the trilayer region. (c) KPFM-scan image of the same area used to delineate the domains. (d) Integrated UPL map (2.4-2.8 eV). Color markers indicating the locations assigned to each polytype (Light blue - ABC, dark blue - CBA, red - ABA and Green - BAB). (e) Full PL spectra under 532 nm excitation, comparing the four polytypes. The main panel shows the known bright excitons emission (X_A , X_B), while the insets highlight the momentum-dark exciton band (X_{Dark}) and the upconverted emission band (X_{Upl}).

two layers, in few-layer 3R-MoS₂ the Q and K valleys are nearly degenerate. Therefore, the formation and recombination of bright excitons from the band edge K/K' valleys is still quite efficient, lowering the efficiency of the EEA with respect to the 2H-MoS₂ case. Within this EEA framework, the upconversion efficiency depends critically on energy and momentum conservation, as well as the density of final states in the Γ conduction manifold. Because our measurements indicate that the dark-exciton reservoir is largely insensitive to the specific rhombohedral polytype (Figure 1e), the pronounced variations in UPL intensity most likely originates from differences in how well the EEA conservation constraints resonate with the density of accessible final states in the Γ conduction manifold. To study this, we performed self-consistent field (SCF) calculations for the relaxed atomic models at the Heyd-Scuseria-Ernzerhof (HSE)¹⁷⁻²⁰ screened-exchange hybrid density functional level of theory (see Methods for details). The resulting band structures (Figures 2c-d) reveal a "Γ conduction cluster" consisting of a manifold of closely spaced conduction bands. A key difference emerges between the two neutral polytypes: compared to BAB, the ABA configuration exhibits an increased energy separation between this Γ cluster and the dark-exciton annihilation energy, $2E_{\text{dark}}$ (see inset). This detuning restricts the phase space for EEA final states, potentially explaining the observed UPL suppression in ABA domain despite the identical surface potential and dark-exciton population.

To test this picture quantitatively, we construct a minimal model guided by Fermi's golden rule. The transition rate is proportional to the squared matrix element times the joint density of states, evaluated at energies satisfying conservation. For EEA feeding a bright population, energy conservation requires $2E_{\text{dark}} = E_{\Gamma\Gamma}^{(i)}$. Finite lifetimes and dephasing broaden this constraint: we evaluate a Lorentzian centered at zero energy mismatch, $L(E_{\Gamma\Gamma}^{(i)} - 2E_{\text{dark}}; \gamma_{\text{EEA}})$, which weights each channel by how well it satisfies energy matching. The subsequent radiative recombination produces a Voigt emission line, centered at the transition energy, arising from homogeneous (γ_{hom}) and inhomogeneous (σ_{inhom}) broadening. Absorbing

weak variations in matrix elements into a global amplitude:

$$I_{\text{pred}}(E) = A \sum_i L(E_{\text{TR}}^{(i)} - 2E_{\text{dark}}; \gamma_{\text{EEA}}) \times V(E - \Delta - E_{\text{TR}}^{(i)}; \sigma_{\text{inhom}}, \gamma_{\text{hom}}), \quad (1)$$

where $E_{\text{TR}}^{(i)}$ are DFT-computed $\Gamma \rightarrow \Gamma_i$ gaps, and Δ accounts for missing many-body corrections. The Lorentzian (centered at zero) assigns weight based on energy mismatch, while the Voigt (centered at $E_{\text{TR}}^{(i)} + \Delta$) produces the spectral line shape. Using a single parameter set ($\Delta = -0.48$ eV, $\gamma_{\text{EEA}} = 0.05$ eV, $\sigma_{\text{inhom}} = 0.04$ eV, $\gamma_{\text{hom}} = 0.03$ eV) across all polytypes, the predicted spectra reproduce the experimental hierarchy (Figure 2b): strongly suppressed ABA compared to BAB intensity. This supports an EEA mechanism governed by sampling of the stacking-sensitive Γ conduction cluster.

Layer- and power-dependent UPL in 3R-MoS₂

Having established the polytype sensitivity of UPL in trilayers, we now examine the evolution of this response across a broader range of thicknesses. We investigate a rhombohedral MoS₂ flake containing regions ranging from 3 to 10 layers, as identified by white-light optical contrast (Figure 3a). To visualize the spatial heterogeneity of the upconversion response, we generated a false-color “RGB” UPL map (Figure 3b). In this map, the red, green, and blue channels correspond to spectrally integrated UPL intensities within three energy windows: R = 2.38–2.53 eV, G = 2.53–2.64 eV, and B = 2.61–2.82 eV.

The thickness-dependent UPL spectra (Figure 3c) reveal a non-monotonic intensity trend. While both UPL and momentum-dark exciton peaks (inset, Figure 3c) redshift with increasing layer number, consistent with the narrowing of the electronic bandgap as thickness increases,²¹ the overall UPL intensity peaks at five layers before decreasing in thicker regions. This behavior can be understood through the resonance condition of the EEA process. In the rhombohedral trilayer, our DFT calculations (see Supporting Information) show that the Γ – Γ transitions are significantly detuned from the EEA energy ($2E_{\text{dark}}$). In this regime, the EEA

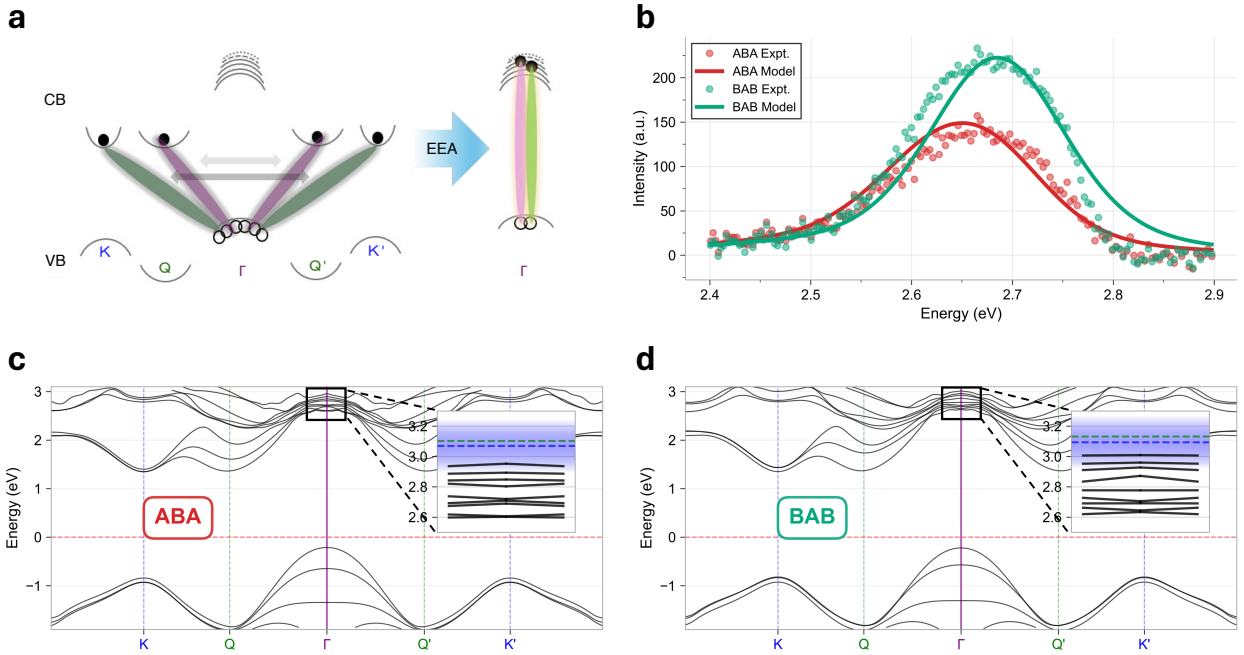


Figure 2: Band-structure origin of polytype-dependent UPL in trilayer 3R-MoS₂. (a) Schematic of the upconversion mechanism: two momentum-dark excitons formed between the Q/Q' (and/or K/K') conduction valleys and the Γ valence band, annihilate into a bright $\Gamma - \Gamma$ exciton, enhanced by the dense cluster of conduction-band states near Γ . (b) Representative UPL spectra of the neutral configurations (ABA and BAB) with experimental data (symbols) and model curves (solid lines), illustrating the polytype-dependent UPL amplitude and lineshape under identical excitation conditions. (c,d) HSE band structures of trilayer ABA and BAB along $K-Q-\Gamma-Q'-K'$. Insets zoom into the conduction-band manifold near Γ and mark the expected two-exciton energies for annihilation channels involving $Q - \Gamma$ dark excitons (green dashed line, $2X_{Q\Gamma}$) and $K - \Gamma$ dark excitons (blue dashed line, $2X_{K\Gamma}$). The shaded band around the blue line indicates the assumed broadening used in the resonance model (shown only for $2X_{K\Gamma}$ to avoid visual overload).

process is less efficient, and a larger fraction of the dark-exciton reservoir decays radiatively at its own energy rather than undergoing upconversion. As the thickness increases toward five layers, the shifting band structure optimizes the energy-matching condition, maximizing UPL efficiency.

To elucidate the underlying many-body dynamics, we performed power-dependent measurements. The resulting spectra imply the UPL line shape is constructed of at least two contributions with distinguished power-law dependencies (see Figure 3d). We modeled these spectra using a decomposition consisting of a low-energy Lorentzian (light gray) and

a higher-energy Fano lineshape (dark gray), both convolved with a Gaussian to account for inhomogeneous broadening (detailed fitting procedures are provided in the Supporting Information). The Fano profile of the high-energy component suggests that the emitting excitonic state interferes with an underlying continuum, likely associated with the dense Γ -conduction manifold.

The two components exhibit markedly different power-law exponents, peak energies, and density-dependent shifts (Figures 3e and 3f). These contrasts can be understood by assigning each component to a distinct dark-exciton annihilation channel. We attribute the high-energy Fano component (triangles) to annihilation of Q – Γ exciton pairs and the low-energy Lorentzian component (squares) to annihilation of K – Γ exciton pairs. Three observations support this assignment. First, the low-energy component displays sub-linear power scaling while the high-energy component shows super-linear scaling that increases from $\alpha \approx 1.5$ in five-layer to $\alpha \approx 3$ in ten-layer (Figure 3e). This behavior is consistent with the disparate density of states in each valley. The K valleys possess only two-fold degeneracy, whereas the Q valleys form a six-fold degenerate ring in momentum space and exhibit heavier effective masses due to their flatter dispersion.^{22–24} These factors suggest that the Q valleys can accommodate a larger exciton population before saturating. The sub-linear scaling of the K – Γ component may indicate that this reservoir approaches saturation within our measurement range, while the Q – Γ channel continues to accumulate excitons and displays the super-linear dependence expected for two-body annihilation. The increase of the power-law exponent with thickness is consistent with the known crossover from exciton-dominated EEA in few-layer TMDs toward more bulk-like Auger recombination, for which the upconversion intensity approaches a cubic scaling.¹⁴ Second, the two components exhibit opposite power-dependent energy shifts (Figure 3f). The high-energy Fano component blueshifts with increasing excitation density, while the low-energy Lorentzian redshifts. This contrast reflects the different interlayer character of the two valleys. The Q valleys are composed of out-of-plane orbitals with strong interlayer coupling and substantial out-of-plane dipole moments, whereas the K

valleys are dominated by in-plane orbitals that remain localized within individual layers.^{24–26} In rhombohedral polytypes, this K -valley confinement is further reinforced by symmetry.²⁷ Q – Γ excitons therefore carry significant dipole moments, evidenced by the density-dependent blueshift, a hallmark of repulsive dipole–dipole interactions between excitons carrying a net out-of-plane dipole moment.^{25,28–30} Finally, the low-energy component consistently appears 30–50 meV below the high-energy component across all measured thicknesses, in agreement with our DFT calculations (see Supporting Information). This energy separation further supports our attribution of the low-energy and high-energy components to the K – Γ and Q – Γ dark-exciton pathways, respectively. This valley-resolved detection highlights a unique spectroscopic capability of UPL. While the momentum-dark exciton band appears as a single feature due to the small energy splitting of excitons from the two valleys, the annihilation process doubles the energy separation and converts the weak dark-exciton emission into a bright upconverted signal. These two factors yield well-resolved spectral components whose distinct power scaling and density-induced shifts can be tracked independently, revealing how polytype variations modulate each valley in ways that remain obscured in direct dark-exciton emission.

Polytype-resolved upconversion in seven-layer 3R-MoS₂

Beyond trilayers, thicker rhombohedral stacks host a richer landscape of local stacking configurations, providing an additional handle to modulate the upconversion response within a single flake. Figure 4 shows a representative seven-layer region of the same rhombohedral crystal. While the optical micrograph (Figure 4a) confirms a uniform thickness, the KPFM map (Figure 4b) reveals multiple lateral domains separated by clear surface-potential steps (line profiles in Figure 4d), consistent with distinct local polytypes at fixed layer number.

UPL spectra acquired at four marked locations (D1–D4) within this seven-layer region (Figure 4c) show the same two-component line shape observed across the thickness-dependent data in Figure 3, comprising a lower-energy component (P1, Lorentzian) and a higher-energy

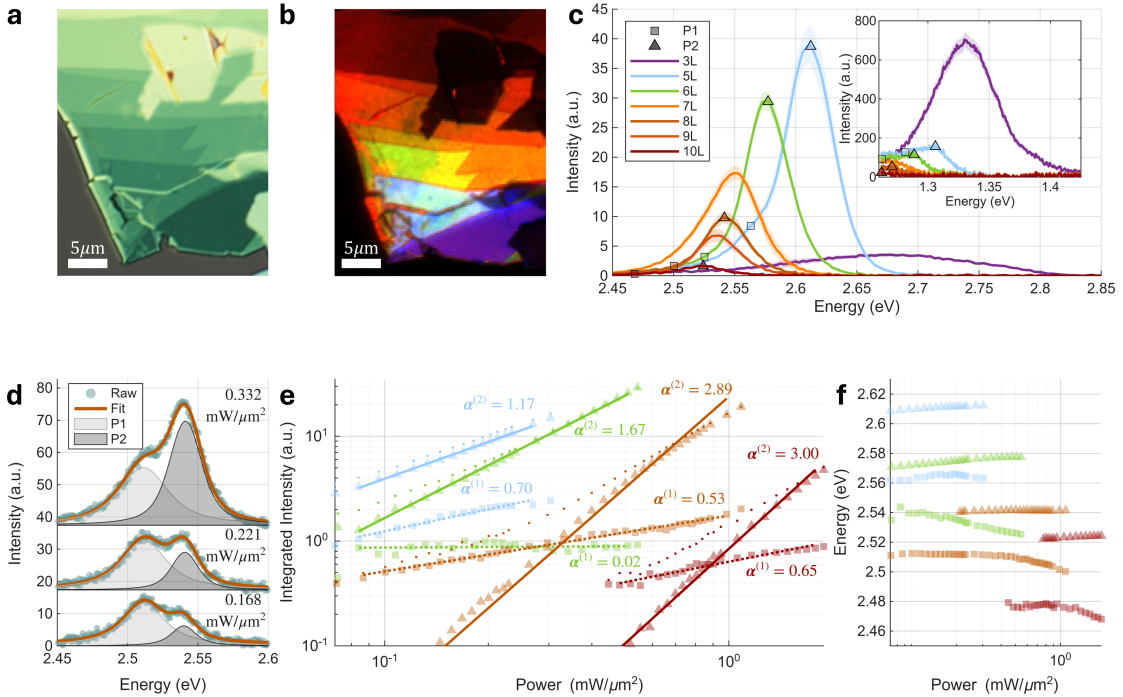


Figure 3: Layer- and power-dependent UPL in 3R-MoS₂. (a) Optical micrograph image of the measured flake. (b) False-color UPL-contrast image of the same area, constructed by mapping the spectrally integrated UPL intensity in three energy windows assigned to the R/G/B channels. Integration bands defined in the main text. (c) UPL spectra from $N = 3$ and $N = 5\text{--}10$ layers, showing a pronounced thickness dependence and two spectral components (P1, P2; peak centers marked). Inset: corresponding momentum-dark exciton spectra. (d) Example spectral fits at three excitation power densities for 6 layers (data, total fit, and two components). (e) Log–log excitation power dependence of the integrated intensity, shown separately for P1 (squares) and P2 (triangles) for each layer number, with power-law fits $I \propto P^\alpha$ (exponents annotated). (f) Extracted peak energies of P1 (squares) and P2 (triangles) versus excitation power.

component (P2, Fano). Importantly, however, the relative amplitudes of these components vary strongly between domains under identical excitation conditions. The brightest domains (D3/D4) show substantially enhanced upconversion compared to the dimmest ones (D1/D2), demonstrating that stacking variations alone can tune the UPL efficiency even when thickness and dielectric environment are held constant.

To quantify this domain-dependent response, we analyze the power dependence of the integrated intensities of P1 and P2 using the same fitting and integration procedure applied in the multilayer data set. Both components behave similarly to the two components discussed in the previous section (Figure 3), following the same two-component spectral structure and comparable power dependence across the measured range (Figure 4e–f). These results show that, at fixed thickness, local stacking alone can reproduce the same spectral trends while strongly modulating the overall upconversion efficiency, making UPL a sensitive probe of polytype variations in thicker 3R-MoS₂.

Conclusion

We have demonstrated the first observation of upconversion photoluminescence in rhombohedral MoS₂, revealing strong sensitivity to stacking configuration. Distinct polytypes within the same flake exhibit markedly different UPL efficiencies, with trilayers providing a clear case where UPL discriminates between the KPFM-degenerate ABA and BAB stackings. Our ab initio-guided analysis attributes this polytype dependence to variations in the Γ -point conduction manifold that governs energy-matching conditions for exciton-exciton annihilation. Furthermore, by combining thickness dependence with component resolved intensity power scaling and density induced energy shifts, we identify two separate EEA channels in the upconversion response and assign them to $K-\Gamma$ and $Q-\Gamma$ dark exciton reservoirs, a distinction that has not been previously established. The annihilation process doubles the energy separation and converts weak dark-exciton emission into a bright signal, resolving

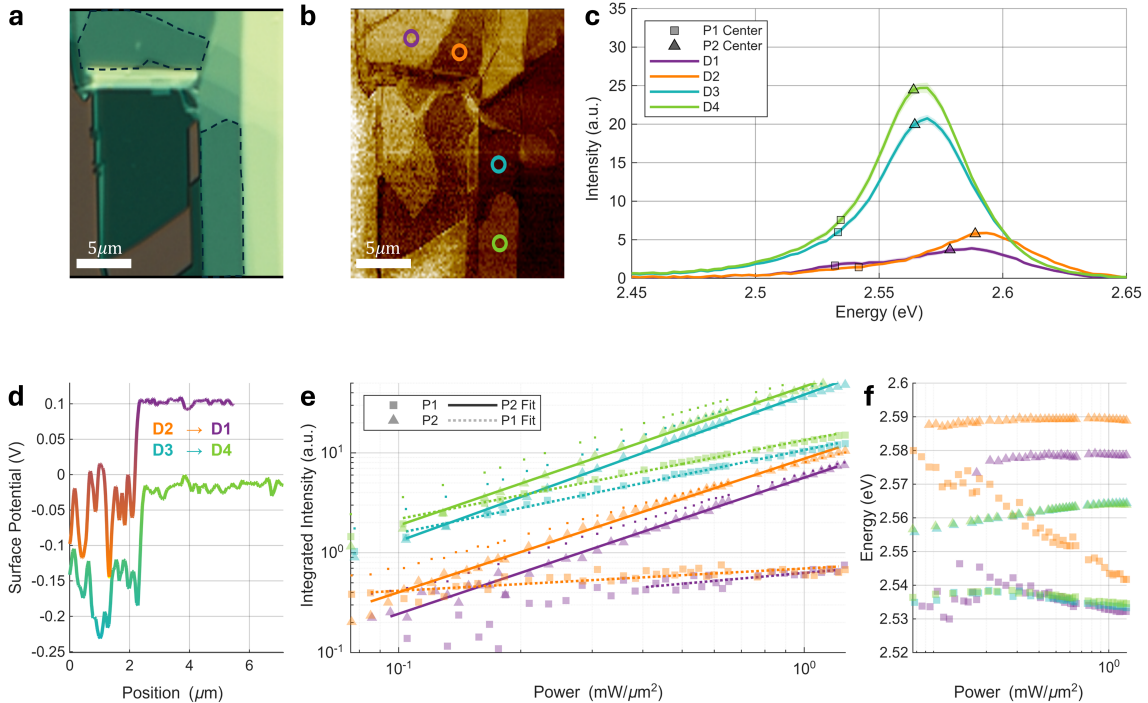


Figure 4: Polytype-dependent UPL in a 7L 3R-MoS₂ region. (a) Optical micrograph of the measured 7L area (dashed outlines). (b) KPFM surface-potential map of the same region, with the four measurement locations (D1–D4, circles) used for the optical spectra. (c) UPL spectra acquired at D1–D4, showing strong domain-dependent intensity at fixed thickness. Symbols mark the extracted centers of the two fitted components (P1 - squares, P2 - triangles). (d) KPFM potential profiles along the straight lines connecting the circles in (b). (e) Log–log excitation power dependence of the integrated intensities of P1 (squares) and P2 (triangles) for each domain, with power-law fits overlaid. (f) Extracted peak energies of P1 (squares) and P2 (triangles) versus excitation power for D1–D4.

contributions that otherwise overlap and providing experimental access to valley-specific responses to stacking order that cannot be obtained through direct dark-exciton spectroscopy. The observation of analogous stacking-selective behavior in seven-layer samples, where multiple polytypes coexist, underscores the generality of this phenomenon. Beyond providing an all-optical readout for ferroelectric domains, these findings establish polytype engineering as a viable route for tailoring upconversion efficiency in 2D semiconductors, with implications for polarization-multiplexed photonics, anti-Stokes light conversion, and the integration of ferroelectric control into nanoscale optoelectronics.

Methods

Device Fabrication

MoS_2 flakes of various thicknesses were mechanically exfoliated from a bulk 3R crystal, ("HQ Graphene"), onto Gel-Pak substrates (DGL-45/17-X8). The thicknesses of 3–10L MoS_2 flakes were calibrated using optical intensity contrast. The MoS_2 flakes on Gel-Pak were transferred onto 90 nm-thick SiO_2/Si substrates at 100 °C.

AFM Measurements

Topography and side-band KPFM measurements were performed using a Park Systems NX10 AFM, employing an HQ:NSC35-Pt tip C with a resonant frequency of ≈ 150 kHz. For side-band measurements, the resonant frequency of the tip was calibrated and then offset by 2.5 kHz. The tip was excited with an AC voltage of 2 V, and oscillation amplitudes of 9 nm to 15 nm were used for all measurements. The images in Fig. 1.c, 4.b were acquired using Park SmartScan software and the data analysis was performed with the Gwyddion program. The stacking order of r- MoS_2 domains (ABC, CBA, ABA/BAB) was determined through systematic analysis of the KPFM measurements. Following the methodology established in our previous work on polar van der Waals heterostructures,⁴ we identify stacking

configurations based on their characteristic surface potential signatures.

Optical characterization

PL spectra were measured using a self-built reflection cryogenic microscope (attoDRY800 with an external objective – LUCPLFLN40X/0.6 NA). Measurements were performed with a linearly polarized 532 nm CW laser. The PL spectra were measured using Shamrock 303i Spectrometer coupled with iDus401 CCD camera (sensor cooled via thermoelectric cooling to 205 K). Optical images of the devices were obtained using a metallurgical microscope.

Computational details

To obtain the electronic structures of multilayered MoS₂, we performed first principles calculations based on density functional theory (DFT), by using Vienna *Ab-initio* Simulation Package (VASP).³¹ The structures were first relaxed, by the Perdew-Burke-Ernzerhof (PBE)³² generalized-gradient exchange-correlation density functional approximation. The interlayer interaction was realized by the Grimme-D3 dispersion correction using Becke-Johnson (BJ) damping.³³ A plane wave energy cutoff of 600 eV and a *k*-point mesh of 20×20×1 were used, with a vertical vacuum size of 2 nm to avoid interactions between adjacent images. The simulation details were similar to the calculations reported in a former work,³⁴ where the convergence tests were done to support the results. Following the structural relaxation, the band structure was calculated at the Heyd-Scuseria-Ernzerhof (HSE) level of theory.

Acknowledgments

M.B.S. acknowledges funding by the European Research Council under the European Union’s Horizon 2024 research and innovation program (“SlideTronics”, consolidator grant agreement No. 101126257) and the Israel Science Foundation under grant No. 319/22 and 3623/21.

H.S. acknowledges funding by the Israel Science Foundation (ISF) Grant No. 2312/21.

References

- (1) Wang, G.; Chernikov, A.; Glazov, M. M.; Heinz, T. F.; Marie, X.; Amand, T.; Urbaszek, B. Colloquium: Excitons in atomically thin transition metal dichalcogenides. *Rev. Mod. Phys.* **2018**, *90*, 021001.
- (2) Xiao, D.; Liu, G.-B.; Feng, W.; Xu, X.; Yao, W. Coupled Spin and Valley Physics in Monolayers of MoS₂ and Other Group-VI Dichalcogenides. *Phys. Rev. Lett.* **2012**, *108*, 196802.
- (3) Vizner Stern, M.; Waschitz, Y.; Cao, W.; Nevo, I.; Watanabe, K.; Taniguchi, T.; Sela, E.; Urbakh, M.; Hod, O.; Ben Shalom, M. Interfacial ferroelectricity by van der Waals sliding. *Science* **2021**, *372*, 1462–1466, Publisher: American Association for the Advancement of Science (AAAS).
- (4) Vizner Stern, M.; Salleh Atri, S.; Ben Shalom, M. Sliding van der Waals polytypes. *Nature Reviews Physics* **2024**,
- (5) Perea-Causin, R.; Erkensten, D.; Fitzgerald, J. M.; Thompson, J. J. P.; Rosati, R.; Brem, S.; Malic, E. Exciton optics, dynamics, and transport in atomically thin semiconductors. *APL Materials* **2022**, *10*, 100701.
- (6) Kizel, I.; Meron, O.; Hershkovitz, D.; Vizner Stern, M.; Ron, A.; Ben Shalom, M.; Suczowski, H. Photoluminescence Detection of Polytype Polarization in r-MoS₂ Enabled by Asymmetric Dielectric Environments. *ACS Nano* **2025**, *19*, 35629–35637.
- (7) Liang, J.; Xie, Y.; Yang, D.; Guo, S.; Watanabe, K.; Taniguchi, T.; Dadap, J. I.; Jones, D.; Ye, Z. Nanosecond Ferroelectric Switching of Intralayer Excitons in Bilayer

through Coulomb Engineering. *Physical Review X* **2025**, *15*, 021081, Published 4 June 2025; CC BY 4.0 license.

- (8) Jones, A. M.; Yu, H.; Schailbley, J. R.; Yan, J.; Mandrus, D. G.; Taniguchi, T.; Watanabe, K.; Dery, H.; Yao, W.; Xu, X. Excitonic luminescence upconversion in a two-dimensional semiconductor. *Nat. Phys.* **2016**, *12*, 323–327.
- (9) Jadcak, J.; Bryja, L.; Kutrowska-Girzycka, J.; Kapuscinski, P.; Bieniek, M.; Huang, Y.-S.; Hawrylak, P. Room temperature multi-phonon upconversion photoluminescence in monolayer semiconductor WS₂. *Nat. Commun.* **2019**, *10*, 107.
- (10) Dai, Y. et al. Phonon-assisted upconversion in twisted two-dimensional semiconductors. *Light Sci. Appl.* **2023**, *12*, 6.
- (11) Manca, M.; Glazov, M. M.; Robert, C.; Cadiz, F.; Taniguchi, T.; Watanabe, K.; Courtade, E.; Amand, T.; Renucci, P.; Marie, X.; Wang, G.; Urbaszek, B. Enabling valley selective exciton scattering in monolayer WSe₂ through upconversion. *Nat. Commun.* **2017**, *8*, 14927.
- (12) Binder, J.; Howarth, J.; Withers, F.; Molas, M. R.; Taniguchi, T.; Watanabe, K.; Faugeras, C.; Wysmolek, A.; Danovich, M.; Fal'ko, V. I.; Geim, A. K.; Novoselov, K. S.; Potemski, M.; Kozikov, A. Upconverted electroluminescence via Auger scattering of interlayer excitons in van der Waals heterostructures. *Nature Communications* **2019**, *10*, 2335.
- (13) Mueller, N. S.; Arul, R.; Kang, G.; Saunders, A. P.; Johnson, A. C.; Sánchez-Iglesias, A.; Hu, S.; Jakob, L. A.; Bar-David, J.; de Nijs, B.; Liz-Marzán, L. M.; Liu, F.; Baumberg, J. J. Photoluminescence upconversion in monolayer WSe₂ activated by plasmonic cavities through resonant excitation of dark excitons. *Nat. Commun.* **2023**, *14*, 5707.
- (14) Chen, Y.-H. et al. Efficient light upconversion via resonant exciton-exciton annihilation

of dark excitons in few-layer transition metal dichalcogenides. *Nat. Commun.* **2025**, *16*, 2879.

(15) Wang, C.; You, L.; Cobden, D.; Wang, J. Towards two-dimensional van der Waals ferroelectrics. *Nat. Mater.* **2023**, *22*, 542–552.

(16) Liang, J.; Yang, D.; Wu, J.; Xiao, Y.; Watanabe, K.; Taniguchi, T.; Dadap, J. I.; Ye, Z. Resolving polarization switching pathways of sliding ferroelectricity in trilayer 3R-MoS₂. *Nature Nanotechnology* **2025**,

(17) Heyd, J.; Scuseria, G. E.; Ernzerhof, M. Hybrid functionals based on a screened Coulomb potential. *J. Chem. Phys.* **2003**, *118*, 8207–8215.

(18) Heyd, J.; Scuseria, G. E. Efficient hybrid density functional calculations in solids: Assessment of the Heyd–Scuseria–Ernzerhof screened Coulomb hybrid functional. *J. Chem. Phys.* **2004**, *121*, 1187–1192.

(19) Heyd, J.; Scuseria, G. E. Assessment and validation of a screened Coulomb hybrid density functional. *J. Chem. Phys.* **2004**, *120*, 7274–7280.

(20) Heyd, J.; Scuseria, G. E.; Ernzerhof, M. Erratum: “Hybrid functionals based on a screened Coulomb potential” [J. Chem. Phys. 118, 8207 (2003)]. *J. Chem. Phys.* **2006**, *124*, 219906.

(21) Zhao, W.; Ribeiro, R. M.; Toh, M.; Carvalho, A.; Kloc, C.; Castro Neto, A. H.; Eda, G. Origin of Indirect Optical Transitions in Few-Layer MoS₂, WS₂, and WSe₂. *Nano Lett.* **2013**, *13*, 5627–5634.

(22) Jin, W.; Yeh, P.-C.; Zaki, N.; Zhang, D.; Sadowski, J. T.; Al-Mahboob, A.; van der Zande, A. M.; Chenet, D. A.; Dadap, J. I.; Herman, I. P.; Sutter, P.; Hone, J.; Osgood, R. M. Direct Measurement of the Thickness-Dependent Electronic Band Struc-

ture of MoS₂ Using Angle-Resolved Photoemission Spectroscopy. *Physical Review Letters* **2013**, *111*, 106801.

(23) Kormányos, A.; Burkard, G.; Gmitra, M.; Fabian, J.; Zólyomi, V.; Drummond, N. D.; Fal'ko, V. *k · p* theory for two-dimensional transition metal dichalcogenide semiconductors. *2D Materials* **2015**, *2*, 022001.

(24) Cheiwhanchamnangij, T.; Lambrecht, W. R. L. Quasiparticle band structure calculation of monolayer, bilayer, and bulk MoS₂. *Physical Review B* **2012**, *85*, 205302.

(25) Jiang, Y.; Chen, S.; Zheng, W.; Zheng, B.; Pan, A. Interlayer exciton formation, relaxation, and transport in TMD van der Waals heterostructures. *Light: Science & Applications* **2021**, *10*, 72.

(26) Kadantsev, E. S.; Hawrylak, P. Electronic structure of a single MoS₂ monolayer. *Solid State Communications* **2012**, *152*, 909–913.

(27) Suzuki, R.; Sakano, M.; Zhang, Y. J.; Akashi, R.; Morikawa, D.; Harasawa, A.; Yaji, K.; Kuroda, K.; Miyamoto, K.; Okuda, T.; Ishizaka, K.; Arita, R.; Iwasa, Y. Valley-dependent spin polarization in bulk MoS₂ with broken inversion symmetry. *Nature Nanotechnology* **2014**, *9*, 611–617.

(28) Kremser, M.; Brotons-Gisbert, M.; Knörzer, J.; Gückelhorn, J.; Meyer, M.; Barbone, M.; Stier, A. V.; Gerardot, B. D.; Müller, K.; Finley, J. J. Discrete interactions between a few interlayer excitons trapped at a MoSe₂–WSe₂ heterointerface. *npj 2D Mater. Appl.* **2020**, *4*, 8.

(29) Federolf, M.; Steinhoff, A.; Emmerling, M.; Florian, M.; Schneider, C.; Höfling, S. Tuning the non-linear interactions of hybrid interlayer excitons in bilayer MoS₂ via electric fields. 2025; <https://arxiv.org/abs/2510.13314>.

(30) Schwandt-Krause, J.; Miloudi, M. E. A.; Blundo, E.; Deb, S.; Heidkamp, J.-N.; Watanabe, K.; Taniguchi, T.; Schwartz, R.; Stier, A. V.; Finley, J. J.; Kühn, O.; Korn, T. Ferroelectric Control of Interlayer Excitons in 3R-MoS₂/MoSe₂ Heterostructures. *Nano Letters* **2025**,

(31) Kresse, G.; Furthmüller, J. Efficient iterative schemes for ab initio total-energy calculations using a plane-wave basis set. *Phys. Rev. B* **1996**, *54*, 11169–11186.

(32) Perdew, J. P.; Burke, K.; Ernzerhof, M. Generalized Gradient Approximation Made Simple. *Phys. Rev. Lett.* **1996**, *77*, 3865–3868.

(33) Grimme, S.; Antony, J.; Ehrlich, S.; Krieg, H. A consistent and accurate ab initio parametrization of density functional dispersion correction (DFT-D) for the 94 elements H–Pu. *J. Chem. Phys.* **2010**, *132*, 154104.

(34) Cao, W.; Deb, S.; Stern, M. V.; Raab, N.; Urbakh, M.; Hod, O.; Kronik, L.; Ben Shalom, M. Polarization Saturation in Multilayered Interfacial Ferroelectrics. *Adv. Mater.* **2024**, *36*, e2400750.